

ANCHORING-INDUCED TEXTURE & SHEAR BANDING OF NEMATIC POLYMERS IN SHEAR CELLS

HONG ZHOU

Department of Applied Mathematics
Naval Postgraduate School, Monterey, CA 93943-5216, USA

M. GREGORY FOREST

Department of Mathematics & Institute for Advanced Materials,
University of North Carolina at Chapel Hill, Chapel Hill, NC 27599-3250, USA

QI WANG

Department of Mathematics
Florida State University, Tallahassee, FL 32306, USA

ABSTRACT. We numerically explore texture (resolved by the second-moment of the orientational distribution) and shear banding of nematic polymers in shear cells, allowing for one-dimensional morphology in the gap between parallel plates. We solve the coupled Navier-Stokes and Doi-Marrucci-Greco orientation tensor model, considering both confined orientation in the plane of shear and full orientation tensor degrees of freedom, and both primary flow and vorticity (in the full tensor model) components. This formulation makes contact with a large literature on analytical and numerical (cf. the review [41]) as well as experimental (cf. the review [45]) studies of nematic polymer texture and flow feedback. *Here we focus on remarkable sensitivity of texture & shear band phenomena to plate anchoring conditions on the orientational distribution.* We first explore steady in-plane flow-nematic states at low Peclet (Pe) and Ericksen (Er) numbers, where asymptotic analysis provides exact texture scaling properties [18, 6]. We illustrate that in-plane steady states co-exist with, and are unstable to, out-of-plane steady states, yet the structures and their scaling properties are not dramatically different. Non-Newtonian shear bands arise through orientational stresses. They are explored first for steady states, where we show the strength and gap location of shear bands can be tuned with anchoring conditions. Next, unsteady flow-texture transitions associated with the Ericksen number cascade are explored. We show the critical Er of the steady-to-unsteady transition, and qualitative features of the space-time attractor, are again strongly dependent on wall anchoring conditions. Other simulations highlight unsteady flow-nematic structures over 3 decades of the Ericksen number, comparisons of shear banding and texture features for in-plane and out-of-plane models, and vorticity generation in out-of-plane attractors.

1. Introduction. Sheared nematic polymers experience a proliferation of texture, in the form of spatial gradients of the orientational distribution of the rod-shaped macromolecules. Cladis & Torza [5] and Manneville [35] described the analogous liquid crystal behavior as director turbulence, while Berry [1] used the term turbidity in his nematic polymer experiments on pristine, nearly homogeneous initial

2000 *Mathematics Subject Classification.* Primary: 82D60, 76A15; Secondary: 65Z05, 35Q99 .
Key words and phrases. Anchoring-induced structure, nematic polymers, shear flow.

Report Documentation Page				Form Approved OMB No. 0704-0188	
Public reporting burden for the collection of information is estimated to average 1 hour per response, including the time for reviewing instructions, searching existing data sources, gathering and maintaining the data needed, and completing and reviewing the collection of information. Send comments regarding this burden estimate or any other aspect of this collection of information, including suggestions for reducing this burden, to Washington Headquarters Services, Directorate for Information Operations and Reports, 1215 Jefferson Davis Highway, Suite 1204, Arlington VA 22202-4302. Respondents should be aware that notwithstanding any other provision of law, no person shall be subject to a penalty for failing to comply with a collection of information if it does not display a currently valid OMB control number.					
1. REPORT DATE OCT 2007		2. REPORT TYPE		3. DATES COVERED 00-00-2007 to 00-00-2007	
4. TITLE AND SUBTITLE Anchoring-Induced Texture & Shear Banding of Nematic Polymers in Shear Cells				5a. CONTRACT NUMBER	
				5b. GRANT NUMBER	
				5c. PROGRAM ELEMENT NUMBER	
6. AUTHOR(S)				5d. PROJECT NUMBER	
				5e. TASK NUMBER	
				5f. WORK UNIT NUMBER	
7. PERFORMING ORGANIZATION NAME(S) AND ADDRESS(ES) Naval Postgraduate School, Department of Applied Mathematics, Monterey, CA, 93943				8. PERFORMING ORGANIZATION REPORT NUMBER	
9. SPONSORING/MONITORING AGENCY NAME(S) AND ADDRESS(ES)				10. SPONSOR/MONITOR'S ACRONYM(S)	
				11. SPONSOR/MONITOR'S REPORT NUMBER(S)	
12. DISTRIBUTION/AVAILABILITY STATEMENT Approved for public release; distribution unlimited					
13. SUPPLEMENTARY NOTES					
14. ABSTRACT We numerically explore texture (resolved by the second-moment of the orientational distribution) and shear banding of nematic polymers in shear cells, allowing for one-dimensional morphology in the gap between parallel plates. We solve the coupled Navier-Stokes and Doi-Marrucci-Greco orientation tensor model, considering both confined orientation in the plane of shear and full orientation tensor degrees of freedom, and both primary flow and vorticity (in the full tensor model) components. This formulation makes contact with a large literature on analytical and numerical (cf. the review [41]) as well as experimental (cf. the review [45]) studies of nematic polymer texture and flow feedback. Here we focus on remarkable sensitivity of texture & shear band phenomena to plate anchoring conditions on the orientational distribution. We first explore steady in-plane flow-nematic states at low Peclet (Pe) and Ericksen (Er) numbers, where asymptotic analysis provides exact texture scaling properties [18, 6]. We illustrate that in-plane steady states co-exist with, and are unstable to, out-of-plane steady states, yet the structures and their scaling properties are not dramatically different. Non-Newtonian shear bands arise through orientational stresses. They are explored first for steady states, where we show the strength and gap location of shear bands can be tuned with anchoring conditions. Next, unsteady flow-texture transitions associated with the Ericksen number cascade are explored. We show the critical Er of the steady-to-unsteady transition, and qualitative features of the space-time attractor, are again strongly dependent on wall anchoring conditions. Other simulations highlight unsteady flow-nematic structures over 3 decades of the Ericksen number, comparisons of shear banding and texture features for in-plane and out-of-plane models, and vorticity generation in out-of-plane attractors.					
15. SUBJECT TERMS					
16. SECURITY CLASSIFICATION OF:			17. LIMITATION OF ABSTRACT Same as Report (SAR)	18. NUMBER OF PAGES 27	19a. NAME OF RESPONSIBLE PERSON
a. REPORT unclassified	b. ABSTRACT unclassified	c. THIS PAGE unclassified			

samples. The present study is motivated by applications to high performance materials; in particular, we are interested in textures generated by thin film or mold processing of nematic polymers and rigid rod nano-composites. The rigid rod inclusions are added to enhance properties, yet the processing-induced variability in the orientational distribution strongly influences conductive and mechanical properties [50, 22, 51, 52, 53, 54]. In particular, film processing of nematic polymers leads to anisotropy (characterized by the local orientational distribution) and heterogeneity (characterized by gradients of the orientational distribution), which are then realized in all properties. The local (monodomain) orientational properties of sheared nematic polymers are now quite well understood; texture generation is in a primitive state by comparison, and in particular the lengthscales of heterogeneity remain very poorly characterized.

Furthermore, non-Newtonian hydrodynamic feedback due to orientational stress leads to shear banding and significant increases in effective viscosity, thereby limiting processability. It is apparently difficult to do velocimetry in nematic polymer flows, and modeling therefore plays an important role in establishing the correlations between texture and flow lengthscales. A remarkable feature predicted by the model simulations reported here is the contrast in shear bands which can form, each with the same mean shear rate across the gap, simply by changing the plate anchoring condition! We find shear bands which have plate layers that move essentially like plug flow with the plates, mediated by a strong shear layer at the center of the gap. Other shear bands have strong shear layers at each plate, and a nearly stationary interior layer. These flow-texture features are the targets of the numerical studies presented, with particular attention to variability in attractors due to anchoring conditions and to steady-unsteady transitions in the Er cascade.

An experimental review of shear behavior and texture formation in nematic polymers is provided by [45], whereas modeling studies on second-moment Landau-deGennes models are reviewed by [41]. The lengthscales of texture, and whether the basic texture modes are extended structures (e.g., span the gap width) or reside in wall boundary layers or defects, remain open questions. What aspects of processing (flow type, flow rate, confinement conditions) generate local and nonlocal texture modes? Information of this type has been inferred from steady state scaling arguments, including seminal work by de Gennes [7], Marrucci and Greco [36, 38] (which led to the Marrucci scaling prediction of $Er^{-\frac{1}{2}}$), Carlsson [3, 4] who argues that wall anchoring effects have a local penetration depth, Larson and Mead [29, 30, 31] (whose experiments and theoretical modeling indicate scaling of Er^{-p} , with $\frac{1}{4} \leq p \leq 1$), all based on the Leslie-Ericksen-Frank small molecule liquid crystal theory. Asymptotic steady scaling analysis of the Doi-Marrucci-Greco second-moment tensor model of liquid crystalline polymers, in the slow flow (low De) and strongly elastic (low Er) limit [18], predicts two types of texture modes: plate boundary layers which obey the Marrucci scaling (dominated by order parameter and director distortions); and nonlocal texture modes (dominated by distortions in the principal axes of orientation) which span the shear gap and obey an Er^{-1} scaling. Furthermore, the strength of the boundary layers is highly sensitive to wall anchoring conditions in this limit, which suggests a critical dependence of order parameter-induced texture on anchoring conditions. Whether this texture remains localized at the plates, as Carlsson deduces from small molecule models, remains an open question for the strong nonlinear interactions in the Doi-Marrucci-Greco model employed here. We provide clear evidence of propagation of wall conditions

throughout the shear gap; in particular, we observe macroscopic bulk flow variability due simply to anchoring conditions.

Numerical confirmation of the asymptotic texture analysis in [18] shows the onset of nonlinear flow feedback, with preliminary evidence that shear band generation is sensitive to anchoring conditions on the orientation tensor. The present study continues these observations with numerical studies at higher Ericksen numbers and with variable in-plane plate anchoring conditions. Our simulations make contact with the predictions of Kupferman et al. [28] of flow generation phenomena; we extend their model two-dimensional (planar) liquid study to three dimensions in orientational space, retaining 1d variation in physical space along the flow-gradient axis spanning the plates. Our confined in-plane simulations are analogous to their 2-dimensional liquid model. The study of out-of-plane anchoring conditions is clearly worth studying, but deferred so we can organize predictions of this multi-parameter study.

There is ample evidence from longwave monodomain studies of several closure models [12], and their comparison with resolved kinetic simulations [19, 20], that a combined mesoscopic closure and kinetic equation approach is prudent. Moving from the longwave limit to structure simulations, the Smoluchowski kinetic solver has been extended to coupled Smoluchowski-Navier-Stokes simulations of one-dimensional structure formation [55, 21]. The Smoluchowski solvers extend the 5 degrees of freedom of the orientation tensor to 65 degrees of freedom of the orientational probability distribution function through a high order spherical harmonic expansion; the number 65 is not magical, rather it is necessary to get converged results. This results in 65 coupled nonlinear reaction-diffusion equations for the orientational distribution; in the coupled Navier-Stokes system, the orientation equations are solved together with the incompressible hydrodynamic equations for the primary velocity and vorticity. Of relevance to the present paper, only limited kinetic parameter runs have been carried out due to extremely high computational costs and numerical limitations of the Smoluchowski-Navier-Stokes model; lengthscales clearly scale with some inverse power of the Ericksen number, but the simulations are too time consuming to deduce scaling exponents. In [55], imposed kinematics and confined in-plane orientational distributions significantly reduce the coupled Smoluchowski-Navier-Stokes system, so that some parameter studies are feasible. Texture phase diagrams reveal parameter domains in Peclet and Ericksen numbers where steady and unsteady attractors prevail, with phase transitions separating the various regions. More limited parameter ranges are explored with full flow coupling and out-of-plane distribution functions [21].

All of these kinetic simulations coupled to Navier-Stokes suggest that qualitative features are well captured by the Doi-Marrucci-Greco tensor model coupled to Navier-Stokes. The present study therefore serves as a coarse-grained approximation and predictor [25] of flow-texture phenomena that can subsequently be confirmed with the high-resolution Smoluchowski-Navier-Stokes codes.

The phenomena of interest for this paper include: texture attractors and associated nonlinear shear band structures; texture phase transitions, between steady and unsteady and between in-plane and out-of plane, consistent with seminal studies of Rey and Tsuji [46, 47]; and a determination of which control parameters trigger the sensitivity or transitions. *The new feature amplified here is the sensitive role of plate anchoring conditions, in modifying flow feedback profiles and texture*

transitions. Our approach is to begin from parameter regimes where we have analytical and numerical benchmarks, namely the low De and Er regime [18], and then to use numerical continuation and systematically document the emergence of new orientational and flow phenomena.

The most resolved Doi-Marrucci-Greco tensor model simulations are the two physical space dimension results from Sgalari, Leal, Feng, Klein, Garcia-Cervera, and Cenicerros [42, 26, 27]. Their studies presume strong anchoring along the vorticity direction, aimed at modeling the roll cell instability [30]. In this paper, we explore plate anchoring at a spectrum of different angles in the flow plane, transverse to the vorticity axis of these 2d studies. The stability of the phenomena reported in this paper to higher space dimensional perturbations, and the study of anchoring conditions between the shear plane and vorticity axis, are topics for the future.

We begin in a parameter regime where asymptotic analysis gives explicit structure formulas and their scaling properties. This is the dual limit of a low Peclet number (sufficiently slow flow) and a low Ericksen number (sufficiently strong elasticity), either with equal bend-splay-twist elasticity constants [18] or with two independent elasticity constants [6]. This slow plate, elasticity-dominated regime characterizes nematic liquids whose distortional elasticity potential is strong enough to arrest all shear-induced tumbling in the interior of the shear cell. Physically, this limit is not realizable except by cooling the liquid, where shear cell experiments may not be possible. In any case, it is a limit that gives important information with which to guide parameter continuation from benchmarked algorithms and controlled lengthscales of flow and orientation.

Analytically, we have derived steady molecular orientational distributions with relatively mild spatial gradients and very weak non-Newtonian flow feedback. The analysis, however, is only tractable when orientational distributions are restricted to *in-plane* major directors, which confines the peak orientation axis to lie in the plane of the flow and flow gradient. We are thus led to first numerically explore the persistence and stability of these asymptotic solutions as the Ericksen and Peclet numbers are raised out of the asymptotic range of validity, but then to also explore behavior inaccessible to analysis: potential co-existence of out-of-plane steady attractors, stability of all steady states, and the possibility of unsteady transitions where steady states no longer exist.

2. Model formulation and the orientation tensor representation. We consider planar shear flow between two plates located at $y = \pm h$, in Cartesian coordinates (x, y, z) , moving with corresponding velocity $\mathbf{v} = (\pm v_0, 0, 0)$, respectively. Variations in the direction of flow (x) and primary vorticity direction (z), and transport in the vertical (y) direction are suppressed. **Figure 1** is a generic parallel plate figure showing a nonlinear shear flow and a spatially varying orientation tensor ellipsoid at several locations between the plates.

The Doi-Hess kinetic theory is developed to study the dynamics of LCP molecules in terms of a probability distribution function. The full orientation tensor theory (Doi-Marrucci-Greco model) is developed after the kinetic theory for the distribution function is projected onto a second-moment description using closure rules. A major ingredient in this tensor theory is the second-moment tensor \mathbf{Q} which describes the mesoscopic orientational distribution of rod-like LCPs:

$$\mathbf{Q} = \langle \mathbf{m} \mathbf{m} \rangle - \frac{\mathbf{I}}{3}, \quad (1)$$

where the angular brackets indicate an average with respect to the probability distribution function, \mathbf{m} is a unit vector representing the direction of a random rodlike molecule, and \mathbf{I} is the identity tensor.

The orientation tensor is related to the *second moment tensor* $\mathbf{M} = \langle \mathbf{m} \mathbf{m} \rangle$ of the probability distribution function of the rod-like molecules by $\mathbf{Q} = \mathbf{M} - \frac{1}{3}\mathbf{I}$. As such, \mathbf{M} is symmetric with non-negative eigenvalues $0 \leq d_3 \leq d_2 \leq d_1 \leq 1$, and trace 1 ($d_1 + d_2 + d_3 = 1$). The orthonormal frame of eigenvectors \mathbf{n}_i with semi-axes d_i determines an ellipsoid at each location and time; spheres correspond to isotropic distributions ($d_1 = d_2 = d_3 = \frac{1}{3}$) with all directions of orientation equally probable, spheroids (with two equal axes) depict uniaxial distributions ($d_1 \neq d_2 = d_3$ are characteristic of stable nematic equilibria) where the peak (most probable) orientation axis \mathbf{n}_1 is called the major director, and full triaxial ellipsoids correspond to biaxial orientation. Each ellipsoid represents a mesophase point, on the order of a cubic micron, containing approximately millions of spheroids. The orientation tensor \mathbf{Q} is the basis for micron-scale light scattering measurements of primary axes (directors) and degrees of molecular alignment (birefringence) and normal and shear stress measurements.

The spectral representation of \mathbf{Q} ,

$$\mathbf{Q} = s(y, t)(\mathbf{n}_1 \mathbf{n}_1 - \frac{\mathbf{I}}{3}) + \beta(y, t)(\mathbf{n}_2 \mathbf{n}_2 - \frac{\mathbf{I}}{3}), \quad (2)$$

recasts the orientation tensor directly in terms of measurable quantities, the mesoscopic directors defined above, and the *order parameters*, $s = d_1 - d_2$, $\beta = d_2 - d_3$, which immediately convey *degrees of anisotropy* of the orientational distribution of the rod ensemble. Uniaxial phases correspond to $s \neq 0$ and $\beta = 0$, $s = 0$ and $\beta \neq 0$, and $s = \beta$, whereas biaxial phases correspond to $s \neq 0$ and $\beta \neq 0$. Whenever $s = 0$ and $\beta = 0$, the major director is not uniquely defined, and such orientational states are called defects. Otherwise, e.g., $s \neq 0$ and $\beta = 0$, a major director is uniquely defined as the most probable axis of rod orientation.

We note for later consideration the geometric form of *confined in-plane orientational distributions*. One director \mathbf{n}_3 is fixed along the vorticity (z) axis, so the remaining directors \mathbf{n}_1 , \mathbf{n}_2 are confined to the (x, y) plane, and thus parametrized by a single angle $\psi(y, t)$,

$$\mathbf{n}_1 = (\cos \psi, \sin \psi, 0), \mathbf{n}_2 = (-\sin \psi, \cos \psi, 0). \quad (3)$$

Model equations

We nondimensionalize the DMG model using the length scale h (gap height) and a time scale t_0 to be specified below. The dimensionless flow and stress variables become:

$$\tilde{\mathbf{v}} = \frac{t_0}{h} \mathbf{v}, \tilde{\mathbf{x}} = \frac{1}{h} \mathbf{x}, \tilde{t} = \frac{t}{t_0}, \tilde{\tau} = \frac{h^2}{f_0} \tau, \tilde{p} = \frac{h^2}{f_0} p, \quad (4)$$

where $f_0 = \rho h^4/t_0^2$ is an experimentally imposed inertial force. The following seven dimensionless parameters arise:

$$\begin{aligned} De &= \frac{1}{6D_r^0 t_0}, Re = \frac{\rho h^2}{t_0 \eta}, \alpha = \frac{3ckTt_0^2}{h^2 \rho}, \\ Er &= \frac{8h^2}{ND_r^0 t_0 l^2}, \mu_i = \frac{3ckT\zeta_i t_0}{h^2 \rho}, i = 1, 2, 3; \end{aligned} \quad (5)$$

α measures the strength of elastic energy relative to kinetic energy; De is the Deborah number for the molecular relaxation rate normalized by shear rate; Re is the solvent Reynolds number; Er is the Ericksen number which measures short-range nematic potential strength relative to distortional elasticity strength; $\mu_i, i = 1, 2, 3$ are three nematic Reynolds numbers, arising from the Miesowicz viscosities relative to plate inertia. We drop the tilde \sim on all variables; all figures correspond to normalized variables and length, time scales.

The balance of linear momentum, stress constitutive equation, continuity equation, and the equation for the orientation tensor in the nondimensional form yield [18]

$$\begin{aligned} \frac{d\mathbf{v}}{dt} &= \nabla \cdot (-p\mathbf{I} + \boldsymbol{\tau}), \\ \boldsymbol{\tau} &= \left(\frac{2}{Re} + \mu_3\right)\mathbf{D} + a\alpha F(\mathbf{Q}) \\ &\quad + \frac{a\alpha}{3Er} \left\{ \Delta\mathbf{Q} : \mathbf{Q}(\mathbf{Q} + \frac{\mathbf{I}}{3}) - \frac{1}{2}(\Delta\mathbf{Q}\mathbf{Q} + \mathbf{Q}\Delta\mathbf{Q}) - \frac{1}{3}\Delta\mathbf{Q} \right\} \\ &\quad + \frac{\alpha}{3Er} \left\{ \frac{1}{2}(\mathbf{Q}\Delta\mathbf{Q} - \Delta\mathbf{Q}\mathbf{Q}) - \frac{1}{4}(\nabla\mathbf{Q} : \nabla\mathbf{Q} - \nabla\nabla\mathbf{Q} : \mathbf{Q}) \right\} \\ &\quad + \mu_1 \left\{ \left(\mathbf{Q} + \frac{\mathbf{I}}{3}\right)\mathbf{D} + \mathbf{D}\left(\mathbf{Q} + \frac{\mathbf{I}}{3}\right) \right\} + \mu_2 \mathbf{D} : \mathbf{Q} \left(\mathbf{Q} + \frac{\mathbf{I}}{3}\right), \end{aligned} \quad (6)$$

$$\nabla \cdot \mathbf{v} = 0,$$

$$\begin{aligned} \frac{d}{dt}\mathbf{Q} &= \boldsymbol{\Omega}\mathbf{Q} - \mathbf{Q}\boldsymbol{\Omega} + a[\mathbf{D}\mathbf{Q} + \mathbf{Q}\mathbf{D}] + \frac{2a}{3}\mathbf{D} - 2a\mathbf{D} : \mathbf{Q}(\mathbf{Q} + \frac{\mathbf{I}}{3}) \\ &\quad - \frac{1}{De} \left\{ F(\mathbf{Q}) + \frac{1}{3Er} \left[\Delta\mathbf{Q} : \mathbf{Q}(\mathbf{Q} + \frac{\mathbf{I}}{3}) \right. \right. \\ &\quad \left. \left. - \frac{1}{2}(\Delta\mathbf{Q}\mathbf{Q} + \mathbf{Q}\Delta\mathbf{Q}) - \frac{1}{3}\Delta\mathbf{Q} \right] \right\}, \end{aligned}$$

where the rate-of-strain tensor \mathbf{D} , the vorticity tensor $\boldsymbol{\Omega}$ and the short-range excluded volume effect $F(\mathbf{Q})$ are given by

$$\begin{aligned} \mathbf{D} &= (\nabla\mathbf{v} + \nabla\mathbf{v}^T)/2, \quad \boldsymbol{\Omega} = (\nabla\mathbf{v} - \nabla\mathbf{v}^T)/2, \\ F(\mathbf{Q}) &= (1 - N/3)\mathbf{Q} - N\mathbf{Q}^2 + N\mathbf{Q} : \mathbf{Q}(\mathbf{Q} + \mathbf{I}/3). \end{aligned} \quad (7)$$

In the above equations \mathbf{I} is the unit tensor; d/dt is the material derivative; a is a dimensionless parameter which depends on the molecular aspect ratio r of spheroidal molecules $a = \frac{r^2-1}{r^2+1}$; N is a dimensionless concentration of nematic polymers, which controls the strength of the mesoscopic approximation, $F(\mathbf{Q})$, of the gradient of the

Maier-Saupe short-range intermolecular potential. We note that the geometry and 1-dimensional assumption kill the convective nonlinearity in the flow equations.

Boundary Conditions

The boundary conditions for the scaled axial velocity v_x are

$$v_x(y = \pm 1) = \pm Pe, \quad (8)$$

where Pe is the Peclet number representing the ratio of the time scale set by the moving plate speed and the characteristic time scale.

We assume *homogeneous mesophase anchoring at the plates*, given by a stable nematic equilibrium,

$$\begin{aligned} \mathbf{Q}|_{y=\pm 1} &= s_0(\mathbf{nn} - \frac{\mathbf{I}}{3}), \\ s_0 &= \frac{1}{4}(1 + 3\sqrt{1 - \frac{8}{3N}}), \end{aligned} \quad (9)$$

where s_0 is the uniaxial order parameter specified by the nematic concentration $N > \frac{8}{3}$, and \mathbf{n} is the equilibrium uniaxial director, assumed to lie in the shear plane (flow-flow gradient plane) at some experimentally dictated *anchoring angle* ψ_0 with respect to the flow direction,

$$\mathbf{n} = (\cos \psi_0, \sin \psi_0, 0). \quad (10)$$

The anchoring angle will appear prominently in the results below; plate preparations yield tangential ($\psi_0 = 0$), homeotropic ($\psi_0 = \frac{\pi}{2}$), or tilted ($0 < \psi_0 < \frac{\pi}{2}$) anchoring. These restricted plate anchoring conditions are relevant for exploring in-plane structures, where we have analytical solutions to benchmark the codes. We show that even with in-plane anchoring conditions, mid-gap molecular ensembles escape the shearing plane if the longwave monodomain dynamics is unstable to out-of-plane orientation. Thus, we gain predictive value for texture simulations from the monodomain phase diagrams and bifurcation diagrams which identify unstable in-plane steady states and limit cycles [12].

Numerical Methods

We solve the system of PDEs (6) numerically using a second-order finite-difference scheme to approximate the spatial derivatives together with an adaptive fourth order Runge-Kutta-Fehlberg time integration method. More precisely, we use hybrid discretization where the orientation tensor and the shear velocity are discretized on staggered meshes. In order to get more resolutions near the channel walls, we map a uniform mesh on a computational coordinate θ ($\theta \in [-1, 1]$) to a non-uniform mesh on the physical y -coordinate ($y \in [-1, 1]$):

$$y(\theta) = \frac{\tanh(\delta \cdot \theta/2)}{\tanh(\delta/2)} \quad (11)$$

where the parameter δ controls the distribution of grid points in the $[-1, 1]$ interval. Our numerical method is similar to the one used in [28].

In this work we assume the velocity is of the form $\mathbf{v} = (v_x(y), 0, v_z(y))$ which automatically satisfies the incompressible condition.

Since we are interested in the steady state solutions, we also solve the corresponding ODEs of (6) by first discretizing the spatial derivatives and then solving the resulting system with Newton's method.

In the simulations presented in this paper, we choose the characteristic time scale as proportional to the LCP relaxation time, i.e., $De = 1$. We also fix $Re = 1000$,

$a = 0.8$, $\mu_1 = 2.3867 \times 10^{-4}$, $\mu_2 = 3.1607 \times 10^{-3}$, $\mu_3 = 3.5 \times 10^{-3}$, and $\alpha = 2$. We fix an equilibrium nematic concentration $N = 6$ and consider structure formation versus 3 control parameters: the plate anchoring angle of the equilibrium director, the Ericksen number Er and the Peclet number Pe . For $N = 6$, the equilibrium order parameter $s_0 = 0.809$, which is the baseline for how well ordered the rod ensemble is throughout the gap. We obtain the steady state solutions by solving the ODE system. When we solve the PDEs, we sometimes use the steady state solutions plus random perturbations as initial conditions and sometimes just start with arbitrary initial conditions. We pay close attention to “director distortions” associated with variations in the principle axes of orientation, versus “molecular elasticity” associated with order parameter gradients which reflect focusing (increase in the order parameter s) versus defocusing (decrease in s) in the orientational distribution. Furthermore, we look for “non-Newtonian flow feedback” in the form of shear bands. Finally, we study correlations between these three features of steady and unsteady attractors.

A note on imposed symmetries: The primary flow profile is constrained by the plate conditions to a mean shear rate equal to the bulk shear rate imposed by the moving plates. At any time, in particular in steady state, the mean flow profile is a simple linear shear, and all flow profiles are odd functions of y . It follows by analysis of the in-plane flow-orientation tensor equations that the in-plane director and order parameters are even functions of y . These symmetries are broken experimentally by slight mismatches in plate speeds and anchoring conditions, but from the point of view of modeling predictions, this choice of symmetric boundary conditions essentially cuts in half the functional degrees of freedom in the flow and orientation tensor. Since a primary purpose of this study is to understand development of new structures and lengthscales, and what material and experimental conditions trigger them, we choose for this study to maintain these symmetries.

We recall that closed-form steady structures are derived in [18] for this model, and in [6] for a more general distortional elasticity potential, both analyses valid in the dual limit of slow flow (low Pe) and high distortional elasticity (low Er). These exact formulas provide guidance for an otherwise daunting, multi-parameter, numerical investigation. Recall the parameter space includes: processing conditions (plate speeds (Pe) which model processing throughput controls, molecular anchoring conditions which model mechanical or chemical wall preparations, plate separation distance which models confinement effects); material properties (nematic polymer concentration, molecular aspect ratio, distortional elasticity); and, timescales on which the nematic polymer liquid is exposed to the flow processing. The analysis has proven tractable so far only for restricted in-plane orientation tensors (with $Q_{xz} = Q_{yz} = 0$).

In the low Pe , low Er regime, we have predictive control over steady, in-plane, flow-nematic properties:

1. the type of LCP structure “modes”: a non-uniform permeation mode that spans the entire gap, dominated by nematic or director-dominated distortions, and boundary layer modes localized at the plates which include molecular elasticity or strong order parameter distortions;
2. the scaling properties of each LCP structure mode, with Er^{-1} mean length scale in permeation modes and $Er^{-1/2}$ length scales in the plate layers; and,
3. the remarkable sensitivity of the amplitudes of order parameter distortions, and thereby the boundary layer structure, to plate anchoring conditions;

4. the velocity profile at leading order is a simple linear shear profile, consistent with a typical assumption in many early studies of nematic polymer structure generation, yet indications that plate anchoring conditions may control the strength and convexity of nonlinear shear band formation.

We begin with numerical results at the parameter boundary where asymptotic analysis provides exact formulas for steady flow-orientation morphology. We focus this section first on confined in-plane steady structure phenomena as we parametrically violate the asymptotic assumptions, and then address out-of-plane steady states. The highlights of each simulation are italicized.

3. The low Ericksen number cascade of steady states for $Pe = 0.5$. **Figure 2** provides the baseline for confined in-plane steady structures, with $Pe = 0.5$ and $Er = 1$. The asymptotic scaling laws [18] accurately predict phenomena seen here; steady structures are given for five different plate anchoring conditions. We summarize the salient features:

- *Nematic elasticity.* The peak axis of alignment (the "Leslie angle" ψ of the major director of \mathbf{Q}), top left panel, agrees with the asymptotic prediction of a parabolic distortion spanning the plates. The major director rotates counterclockwise from the lower plate to the mid-gap, then unwinds back to the top plate. The "degree of nematic distortion", measured by the total variation of the Leslie angle, $\langle |\partial\psi/\partial y| \rangle = |\psi(0) - \psi(\pm 1)|$, is proportional to the anchoring angle ψ_0 .
- *Molecular elasticity.* The order parameters remain close to their equilibrium boundary values ($s = s_0$ and $\beta = 0$), indicating very weak molecular elasticity. Nonetheless, one observes a clear *anchoring dependence on the amplitudes of order parameter variations*, with the strongest response for homeotropic anchoring ($\psi_0 = \pi/2$).
- *Flow-feedback.* The primary flow (lower right panel) is almost identical to pure linear shear for tangential anchoring, but then acquires *weak, twin shear bands*, one on each half of the gap, *triggered only by anchoring variations*.

Figure 3 retains low plate speeds, $Pe = 0.5$, while raising Er by one order of magnitude, from 1 to 10, to reflect slight softening of the strong elastic constant. The salient features are:

- *Nematic elasticity.* Increased rotation of the major director from plate to plate (top left panel), as expected for two reasons: the softer elastic constant offers less resistance to elastic distortions, and asymptotic analysis predicts Er^{-1} scaling of director distortions.
- *Molecular elasticity.* Localized distortions in the order parameters appear to correlate with strong interior shear layers and also with plate layers even if the local flow is plug-like.
- *Flow-feedback phenomena.* The strength and concavity (explained below) of the twin shear bands are strongly modified by the plate anchoring condition. We amplify this anchoring-sensitive steady flow phenomenon:

- For tangential anchoring, strong localized shear layers form at each plate, while the majority of the shear gap is nearly at rest (a slow nearly plug flow layer)!
- Normal anchoring leads to a "flow inversion": approximate plug flow in large layers from each plate to the interior, with a strong shear layer in the mid-gap!

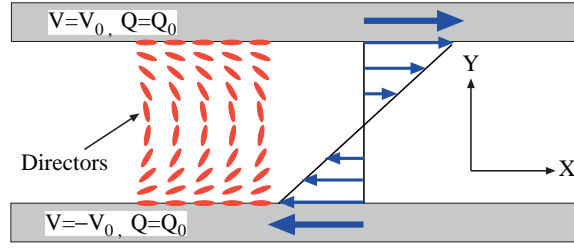


FIGURE 1. A schematic of the parallel plate experiment, with no slip velocity conditions and strong anchoring (tangential in the figure) at the plates. The flow profile depicted is simple shear, with a key focus in simulations to follow on the non-Newtonian flow feedback due to the rigid-rod macromolecular ensemble. The ellipsoids which distort and rotate between the plates depict key features of the orientation tensor \mathbf{Q} at a micron-scale resolution. The eigenvectors of \mathbf{Q} determine the principal axes, with the major director associated with the peak axis of orientation, and differences of the eigenvalues determine the anisotropy in the orientational distribution, which is reflected in the aspect ratio of the ellipsoid.

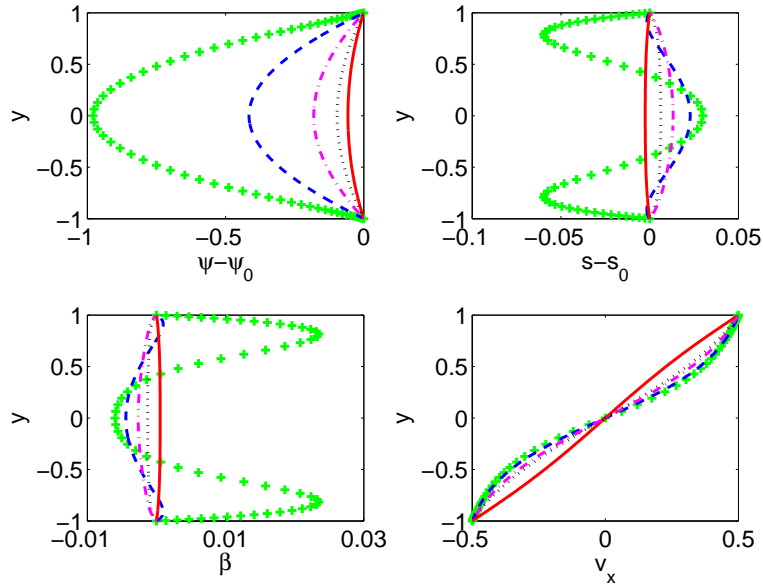


FIGURE 2. The steady ODE solutions with 5 different anchoring conditions. Here $Pe = 0.5$, $Er = 1$. The anchoring angle ψ_0 (in radian measure) for each case is: $\psi_0 = 0$ (solid line), $\pi/16$ (dotted line), $\pi/8$ (dashdot line), $\pi/4$ (dashed line), $\pi/2$ (++) line). Here $s_0 = 0.8090$.

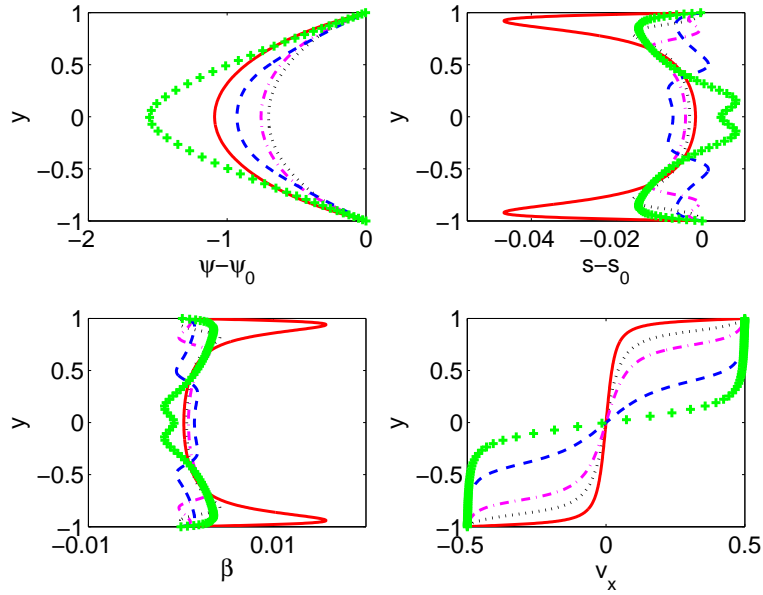


FIGURE 3. The steady ODE solutions with 5 different anchoring conditions. Here $Pe = 0.5$, $Er = 10$. The anchoring angle ψ_0 for each case is: $\psi_0 = 0$ (solid line), $\pi/16$ (dotted line), $\pi/8$ (dashdot line), $\pi/4$ (dashed line), $\pi/2$ (++) line).

- As the anchoring angle varies, the flow profile smoothly interpolates between these two extremes. The width of the plate plug layers scales with the anchoring angle, while plate shear layers grow in intensity as the anchoring angle becomes tangent to the plates. Thus, *the bulk steady nonlinear flow profile is tunable by wall anchoring conditions!*
- *Correlations between flow and orientation tensor structure.*
 - Strong shear layers appear always to generate molecular elasticity. In these steady states, order parameter variations arise where there is a high local Peclet number ($\partial v_x / \partial y$). This means that flow regions of high shear will create full tensor distortions.
 - Order parameter distortions also can arise in regions of a nearly zero local Peclet number, a new feature not hinted from the asymptotic scaling analysis. In the normal anchoring steady state profiles, order parameter variations arise in the near-wall plug layer; they appear to be the first sign of a long-range full tensor structure associated with non-parabolic director scaling (discussed next).
 - The correlation between nematic (director) distortions and flow is more subtle. From asymptotic analysis at low $Er * Pe$, we know that parabolic director profiles proportional to $Er(y^2 - 1)$ coincide with simple linear shear with strength Pe . In asymptotic structures, the order parameter variations are weaker, $O(Pe^2)$. For all but the normal anchoring condition of Figure 3, this parabolic structure prevails. Note however that the director profile for normal anchoring is clearly non-parabolic, with almost

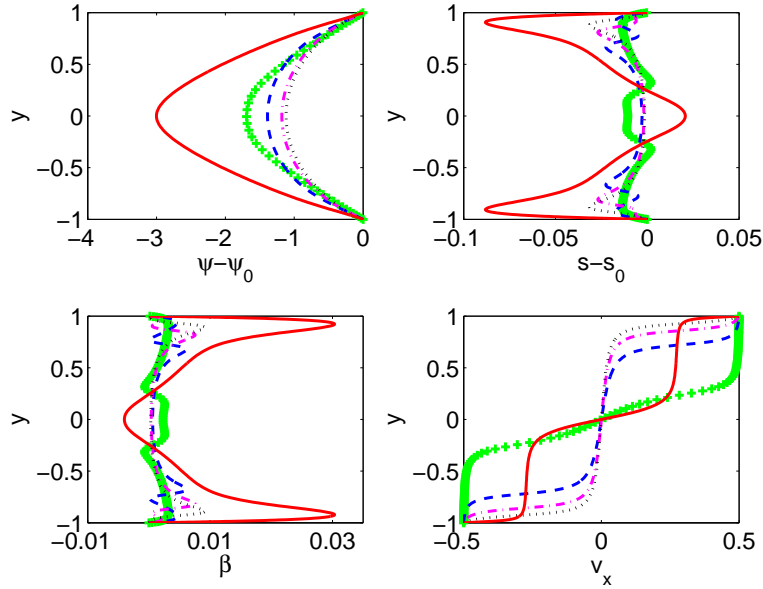


FIGURE 4. The steady ODE solutions with 7 different anchoring conditions. Here $Pe = 0.5$, $Er = 15$. The anchoring angle ψ_0 for each case is: $\psi_0 = 0$ (solid line), $\pi/16$ (dotted line), $\pi/8$ (dashdot line), $\pi/4$ (dashed line), $\pi/2$ (++) line).

linear variation in the plug layers at the plates, and a stronger than quadratic scaling (perhaps $(y^2 - 1)^2$) in the mid-gap where the strong shear layer is.

This flow-tensor steady state suggests that the location of the shear layer relative to the plates plays a major role in director distortions. Namely, when shear layers occur in the interior, then the director is free to distort and is only inhibited by the strength (Er^{-1}) of the distortional elasticity potential. However, when shear layers occur near the plates, the strong anchoring condition suppresses director tumbling for some distance away from the plates; this forces the steady state balance to be achieved predominantly by order parameter distortions.

- Secondary shear band generation in the Er cascade for tangential anchoring

In **Figure 4** we raise Er from 10 to 15, retaining $Pe = 0.5$, and observe persistent in-plane steady states for all ψ_0 between 0 and $\pi/2$, highlighted by:

- *Nematic elasticity.* Comparing Figures 3 & 4, director distortions increase consistent with the asymptotic scaling Er^{-1} , remaining qualitatively similar.
- *Molecular elasticity.* Once again, order parameter gradients arise in strong shear layers.
- *Flow feedback.* We observe a *secondary shear band generation phenomenon* for tangential anchoring, and evidence of the onset of a second shear band with normal anchoring. All flow structures develop stronger nonlinear features, but the tilted anchoring flow profiles develop stronger and more localized shear

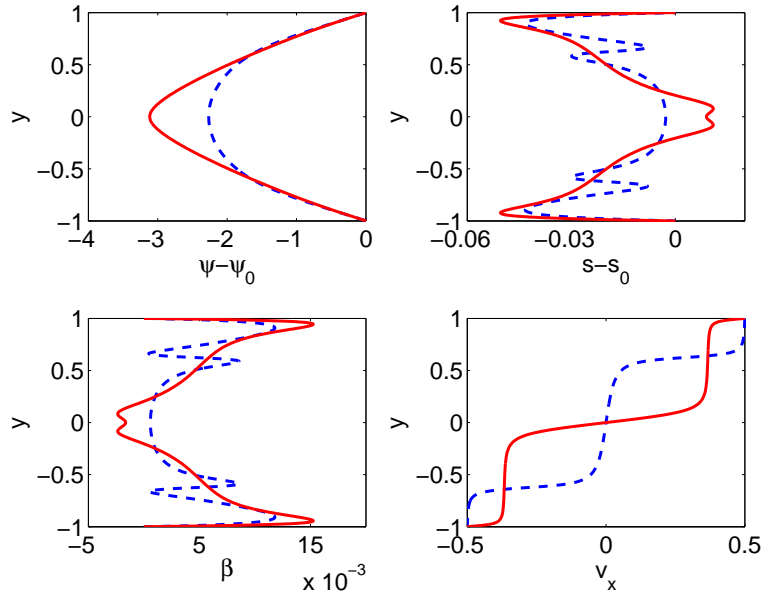


FIGURE 5. The steady ODE solutions with 2 different anchoring conditions. Here $Pe = 0.5$, $Er = 20$. The anchoring angle ψ_0 for each case is: $\psi_0 = 0$ (solid line), $\pi/2$ (dashed line).

layers at the plates for $Er = 15$, with a large interior stationary (plug) layer where the local shear rate is quite small.

We amplify the shear band comparison between the strongest shear layer structures (tangential and normal anchoring) at $Er = 10$ and 15.

- For $\psi_0 = \pi/2$, a second interior shear band has formed at the mid-gap, replacing the previous sharp linear interior layer at $Er = 10$. This localized shear band generation is similar to the full shear gap phenomenon at $Er = 1$ (Figure 2).
- We infer a threshold criterion for linear shear layer strength, above which a nonlinear shear band is generated within the spatial scale of the former linear shear layer. The shear band is accompanied by a parabolic director angle distortion and by order parameter fluctuations, each localized to the spatial extent of the new shear band.
- For tangential anchoring, the flow profile is more dramatic. The strong shear layers at each plate undergo a sharp transition: the number of shear bands jumps from one to two, and each of the four strong linear shear layers are now half as strong as the previous two layers. The $Er = 10$ full flow profile has essentially been duplicated at $Er = 15$ in each half of the gap. The large interior stationary layer is gone, replaced by twin plug flow layers in each half of the gap.
- The order parameters exhibit stronger variations in the double shear band structure, with orientational defocusing near the plates. Thus, lengthscales of

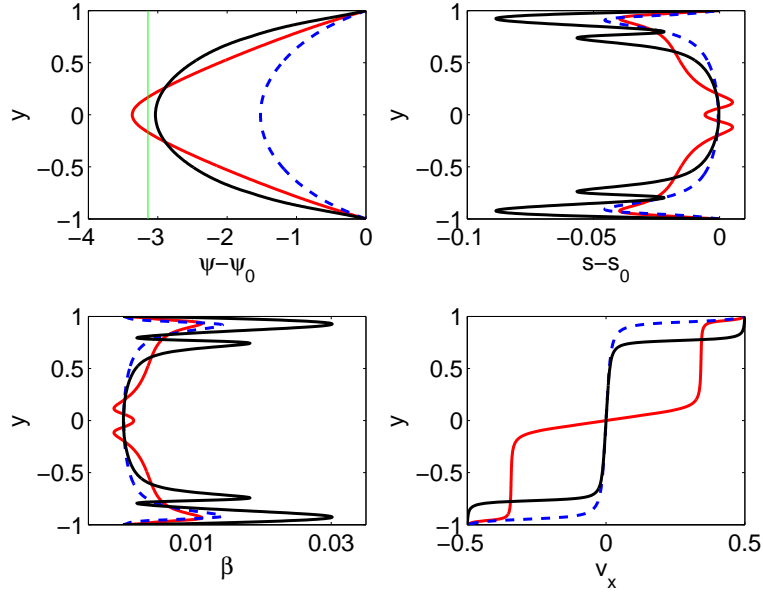


FIGURE 6. The steady ODE solution with 2 different anchoring conditions. Here $Pe = 0.5$. Tilted anchoring $\psi_0 = \pi/16$: $Er = 30$ (solid red line), $Er = 20$ (dashed blue line); Normal anchoring $\psi_0 = \pi/2$: $Er = 30$ (solid black line). Steady state solutions corresponding to anchoring conditions $\psi_0 = \pi/8$ and $\pi/4$ exist (not plotted here). For $\psi_0 = 0$ and $Er = 30$, both the PDE codes and ODE codes indicate that there is no steady state solution. The solid straight line is given by $\psi - \psi_0 = -\pi$.

molecular elasticity appear to correlate with the local normalized shear rate (Deborah number).

Secondary shear band generation was explored in detail in model 2-dimensional liquids by Kupferman et al. [28], using a similar Doi-Marrucci-Greco model. The 2d in space, 2x2 orientation tensor model also restricts to 1d structure between the plates; their 2x2 tensor orientation model is analogous to our in-plane restriction of the 3x3 orientation tensor. They restricted their simulations to parallel wall anchoring, which always generates strong shear layers at the plates (their “burst” phenomenon), so comparisons are restricted to this anchoring condition and the associated Ericksen number cascade phenomena. Kupferman et al. observe strong correlations between shear band generation and the winding number of the planar Leslie angle $\psi(y, t)$, which are *not preserved* by starting from a 3d model and projecting onto 1d in space and in-plane orientation. In the Kupferman et al. simulations, there is essentially a 1:1 correlation between the winding number of the major director (or, nematic distortional bands and lengthscales) and the number of shear bands (or, the lengthscale of each shear band). The top left panel of Figure 4 shows the total variation in ψ still below π , yet shear band structure has already appeared; indeed, shear banding behavior and transitions occur within a winding event of the major director, and appear to correlate with molecular elasticity

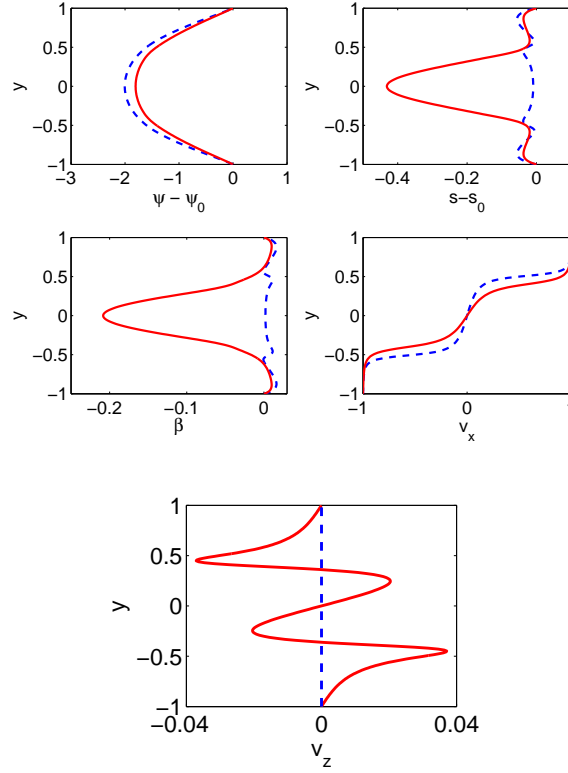


FIGURE 7. The out-of-plane (solid line) and the in-plane (dashed line) steady state solutions with normal anchoring condition where $Pe = 1$ and $Er = 10$.

more than nematic (director) distortions. The viscous-elastic stress communication and non-Newtonian flow feedback are partially captured by this 2d liquid analogy: qualitative features of shear band generation, director spatial distortion scale that decreases with increasing Er , and the steady-unsteady transition we come to below. Yet, other key features are either not accurate (nematic elasticity-shear band correlations) or inaccessible (instability to out of plane orientation, studied below). Of course, both studies require stability analysis and simulation to higher dimensional perturbations in space, which remain unaddressed here.

- Secondary shear band generation in the steady-state Er cascade for normal anchoring

Next, we raise Er from 15 to 20 in **Figure 5**, holding $Pe = 0.5$. Tilted anchoring steady states develop stronger plate shear layers, and increased biaxiality in the orientational distribution, but flow and director features are similar. That is, the flow field has not yet developed twin shear bands with tilted anchoring. We omit these tilted anchoring solutions, deferring to a higher Er simulation presented below (Figure 6), in order to contrast normal versus tangential anchoring at $Er = 20$.

- For tangential anchoring, the double shear band structure of Figure 4 persists, with strengthening of the mid-gap shear layer, weakening of the plate shear

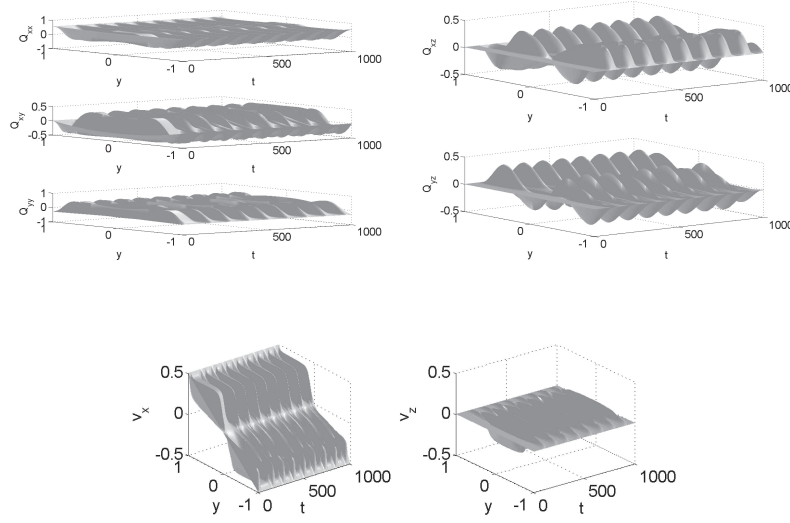


FIGURE 8. The out-of-plane PDE solutions with tangential anchoring condition where $Pe = 0.5$ and $Er = 30$.

layers, and the twin plug flow layers have accelerated toward the plate speed. I.e., the double shear bands have strengthened with increased Er .

- For normal anchoring, the weakly nonlinear interior shear band of Figure 4 has amplified into a strong interior shear band, now consisting of a full gap, twin shear band structure. The plate plug-flow layers of Figure 4 have been compressed to nearly half-width.
- Twin shear band comparison between normal and tangential anchoring

Twin shear bands form for each anchoring condition, with 2 distinctions: (i) they are delayed to higher Er for normal anchoring; and (ii) the shear bands are remarkable distinct. The plug flow layers *either* start at the plates (with normal anchoring) interlaced with strong interior shear layers and plug layers, *or* strong shear layers emanate directly from the plates (with tangential anchoring). *Plate and interior layers switch between plug flow and strong shear layers, due solely to switching of plate anchoring angle.* This is a repeat of the observations in Figure 3 at $Er = 10$ with a single shear band structure. Thus, bulk flow properties appear to consist of shear and plug layer components, whose strengths are picked by Pe , Er values, but the gap location of the components can be switched by changing between tangential and homeotropic anchoring.

- Correlations between director distortions and shear bands for tilted anchoring

We move now to tilted anchoring phenomena, which in asymptotic limits of low Er and Pe consist of enhanced molecular elasticity in plate boundary layers [18, 6].

Figure 6 shows the single-to-double shear band transition for a fixed tilted anchoring condition, $\psi_0 = \pi/16$. The $Er = 20$ steady state solution in dashed blue is a sharper version of the flow profile for tilted anchoring in Figure 4, $Er = 15$. For $Er = 30$, the sharp gradient exceeds an apparent threshold condition, generating the double shear band in red, which reproduces the tangential anchoring flow structure

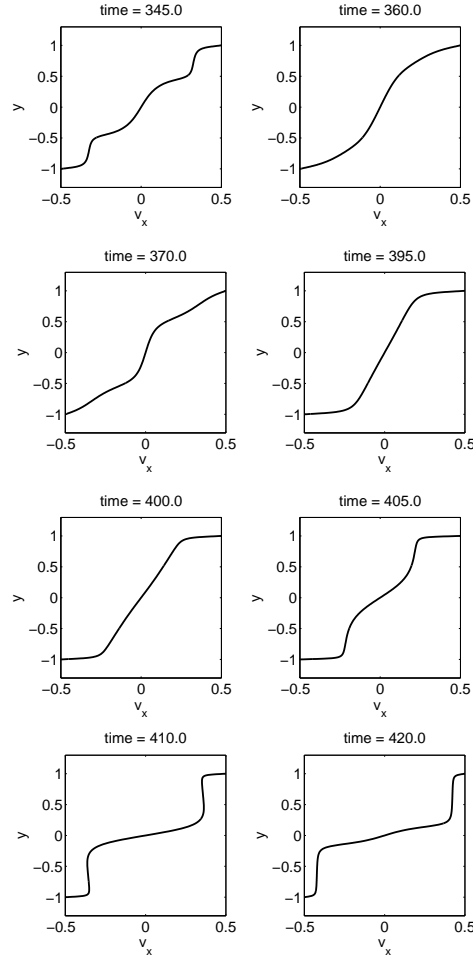


FIGURE 9. Eight snapshots of flow profiles across the gap corresponding to Fig. 8.

at lower $Er = 20$. Thus, *Er-induced shear banding transitions are delayed to higher Er by tilted anchoring, and the relative locations in the gap of plug and shear layers appear to be tunable by plate anchoring condition.*

- Correlations between order parameter distortions and shear bands for parallel and normal anchoring

Figure 6 further shows spatial correlations between shear bands and order parameter distortions. Observe the onset, at $Er = 30$ and normal anchoring, of significant defocusing (lower s) of the orientational distribution and strong biaxiality (non-zero β). This drop in the primary order parameter s is a precursor to defect generation (s near 0) at high Er . Note also that the director distortion has exceeded one complete rotation for the tilted anchoring condition, but not for normal anchoring, and yet both in-plane steady states at $Er = 30$ have spawned twin shear bands. This again shows *the major director winding number is purely coincidental in generation of secondary shear bands.*

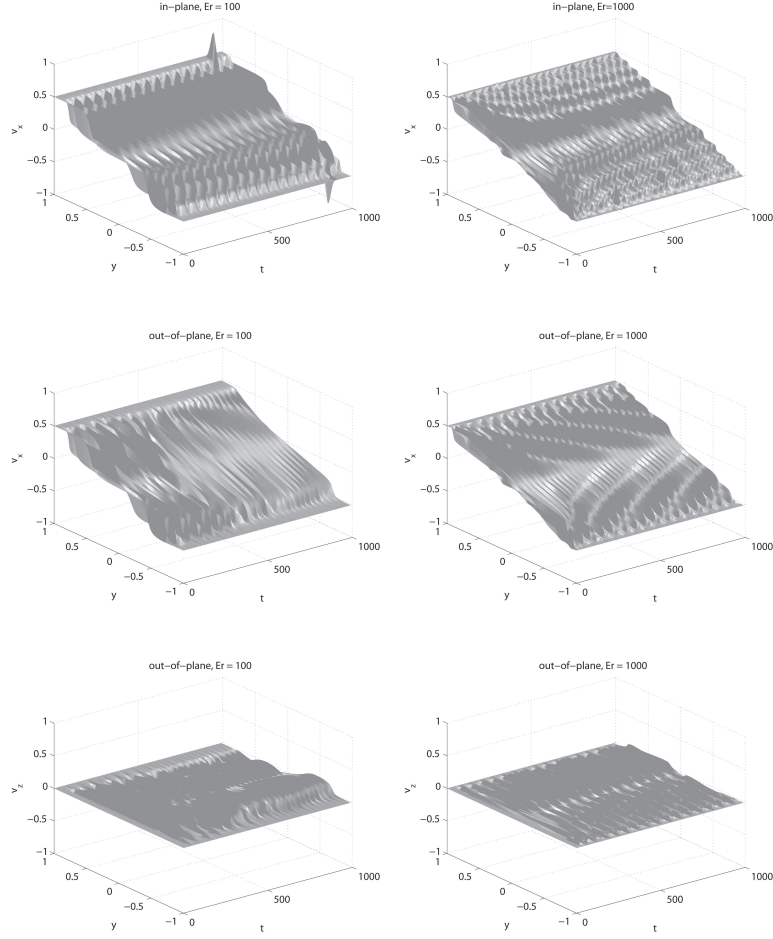


FIGURE 10. The in-plane and out-of-plane PDE solutions for normal anchoring condition where $Pe = 0.5$.

4. Co-existence of out-of-plane steady structures. The asymptotic analysis of the slow plate (low Pe) limit is only tractable for in-plane orientation tensors. The above steady states have confirmed the asymptotic solutions and the scaling behavior at low Pe and Er , and tracked the evolution of the flow and in-plane orientation structures by numerical continuation well beyond the asymptotic regime as Er is increased for $Pe = 0.5$. New structure features on new lengthscales have been identified in the process, in particular shear band generation at some critical Er which is strongly dependent on the boundary anchoring condition; the strong shear layers correlate with orientation order parameter fluctuations and thus focusing and defocusing of the rod distribution function. Only at higher Er do we observe significant departure from the parabolic director winding across the gap.

We now explore other steady structures for which explicit analysis has thus far eluded us, namely nematic structures with out-of-plane orientational degrees of freedom, whose major director is free to roam out of the shear plane (flow-flow gradient

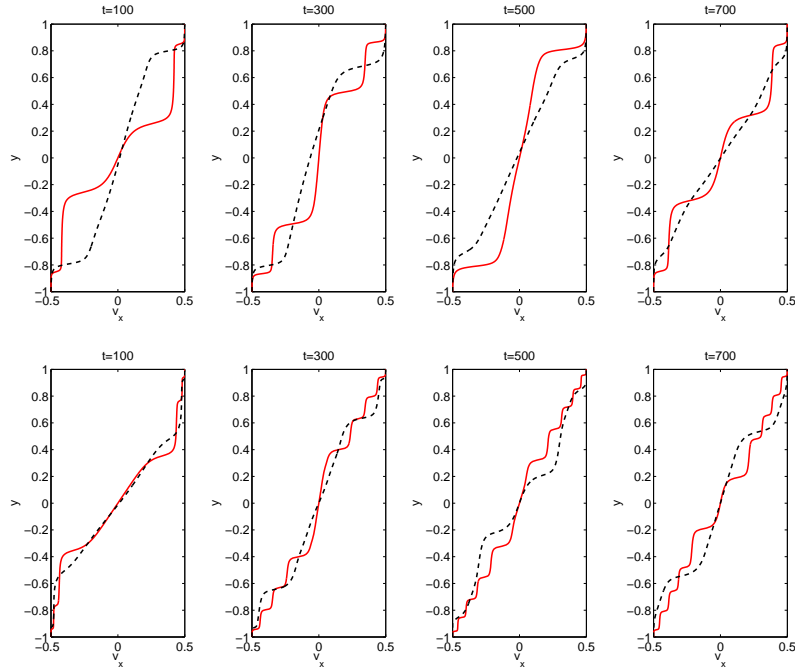


FIGURE 11. Four snapshots of flow profiles across the gap corresponding to Fig. 10. Top panel: $Er = 100$; Bottom panel: $Er = 1000$. In-plane solutions are plotted in solid red lines whereas out-of-plane solutions in dashed black lines.

plane). Below, we will further explore unsteady structures, which may either co-exist with steady structures, or emerge as steady states fail to exist. We are guided in our structure simulations by the longwave limit of homogeneous monodomains, which applied to zero wavenumber dynamics. Recall from [12], at the nematic concentration ($N = 6$) imposed here, the low Pe bulk dynamics consists of in-plane tumbling orbits and out-of-plane kayaking orbits, where the tumbling orbits are unstable to kayaking attractors. Thus, any noisy out-of-plane perturbations across the gap will seed out-of-plane degrees of freedom at any local gap height. Even with distortional elasticity and spatial gradients across the plate gap, there is no apparent mechanism to suppress this longwave instability and drive the full coupled flow-nematic system back to in-plane steady states. The upshot of this argument is that we expect there to be co-existence of steady states (as with monodomains) and steady-unsteady transitions (as with monodomains), since those longwave bifurcations are fully at play in the partial differential equations explored here.

Numerical solutions for $Pe = 1$, $Er = 10$ with a normal and tilted anchoring condition reveal that in-plane steady state solutions are stable, in fact the unique attractor, for confined in-plane simulations. These steady states are unstable in the out-of-plane system, and converge to a steady, out-of-plane flow-nematic structure which is a global attractor. These two co-existing structures are shown in **Figure 7**. We highlight the key features:

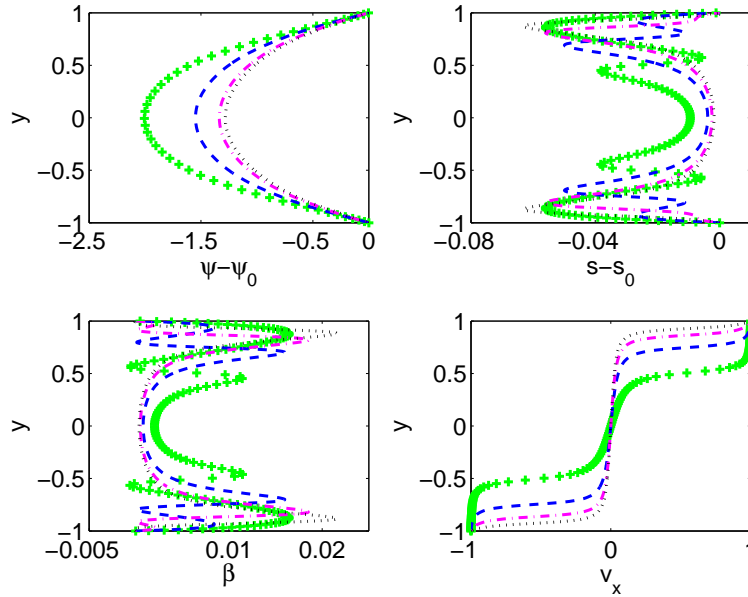


FIGURE 12. The steady ODE solutions with 5 different anchoring conditions. Here $Pe = 1$, $Er = 10$. The anchoring angle ψ_0 for each case is: $\pi/16$ (dotted line), $\pi/8$ (dashdot line), $\pi/4$ (dashed line), $\pi/2$ (++) line). For $\psi_0 = 0$, both the PDE codes and ODE codes indicate that there is no steady state solution.

- *Nematic elasticity.* There is no discernible difference in the in-plane major director rotation across the gap. The out-of-plane attractor is kayaking (in space!), so along with this rotation is a polar angle fluctuation.
- *Molecular elasticity.* The in-plane order parameter distortions are almost negligible, whereas the stable out-of-plane structure has a significant defocusing of the orientational distribution in the center of the gap, along with strong biaxiality.
- *Flow feedback.* The primary shear band structure is qualitatively unchanged in the stable out-of-plane attractor, although clearly there is a softening of the sharp shear layers. The vorticity generation is evident, most prominent at the shear layers.
- *Flow-nematic correlations.* The director distortions do not have signatures across the gap that correlate with other features. The in-plane solutions suppress any measurable spatial correlations. On the other hand, there are clear correlations in the out-of-plane attractor between molecular elasticity, shear bands, and vorticity generation.

5. Unsteady structure transitions and sensitivity to anchoring conditions.

5.1. Anchoring-dependent loss of in-plane steady states. For $Pe = 0.5$, $Er = 30$ and tangential anchoring, we fail to find steady states. Recall (Figure 6) that other anchoring angles produce in-plane steady structures at $Er = 30$, and

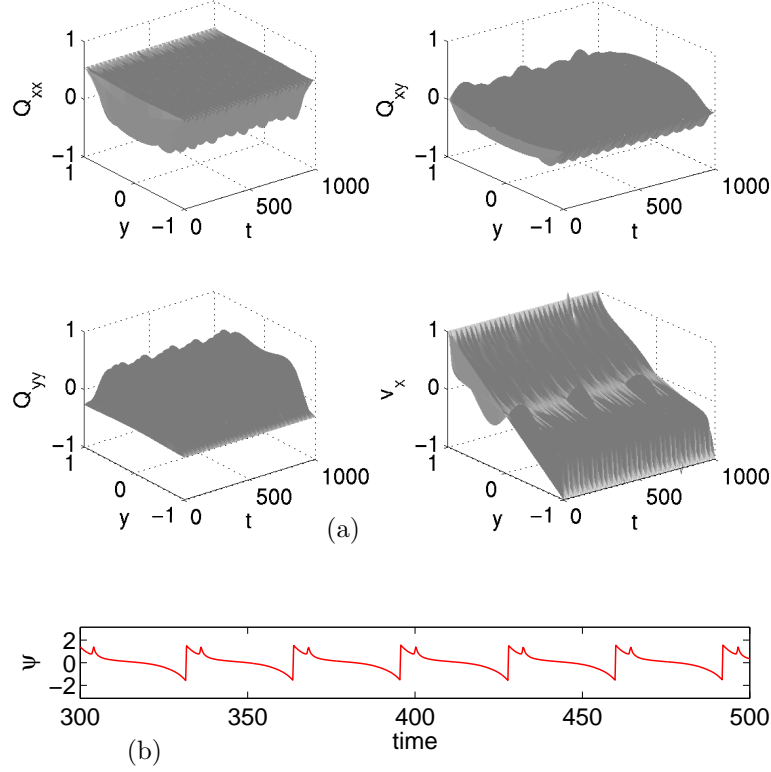


FIGURE 13. Unsteady out-of-plane simulation for parallel anchoring with $Pe = 1.0$, $Er = 10$, and noisy initial data in v_z , Q_{xz} , Q_{yz} . The secondary vorticity and out-of-plane \mathbf{Q} components quickly saturate to zero (not shown), marking convergence to an *in-plane, spatio-temporal attractor*. Top 4 panels: the in-plane \mathbf{Q} tensor components and primary velocity component. Bottom panel: Time evolution of the in-plane Leslie angle ψ at the mid-plane.

tangential anchoring has steady states at $Er = 20$. In graphs not shown here, the shear layers continue to steepen as Er increases between 20 and 30; rather than spawn yet another pair of shear bands, a different transition emerges which is not accessible by the in-plane steady code. We therefore turn to *two possible consequences of loss of in-plane steady state solutions*: either an in-plane to out-of-plane steady state transition, or a steady-to-unsteady transition (which could be either in-plane or out-of-plane). All evidence thus far indicates that in-plane and out-of-plane steady states co-exist (Figure 7), and that both states simultaneously undergo an unsteady transition as either the Ericksen number or Peclet number is raised. Furthermore, the critical Er and Pe of these transitions are strongly dependent on the plate anchoring angle. We will not exhaust this 3 parameter space in this paper, instead showing examples of these transition phenomena.

Figure 8 shows the space-time attractor from the PDE flow-structure simulation with $Er = 30$, $Pe = 0.5$, and tangential anchoring, where the out-of-plane tensor

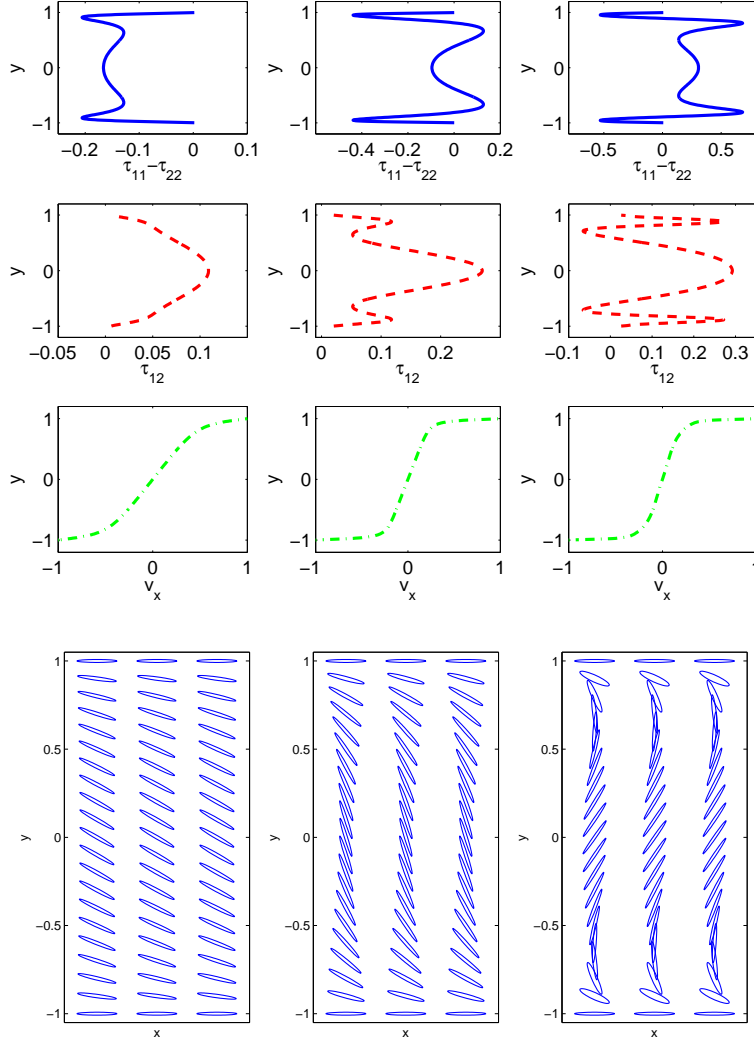


FIGURE 14. The first/second normal stress differences ($\tau_{11} - \tau_{22}$), shear stress (τ_{12}), velocity component v_x , and orientation tensor ellipsoids across the plate gap for 3 snapshots $t = 320$ (left column), $t = 325$ (middle column), $t = 330$ (right column) of the spatio-temporal “wagging structure attractor” of Fig. 13.

components Q_{xz} and Q_{yz} are clearly nonzero, and the vorticity likewise is nonzero. **Figure 9** gives 8 snapshots of the flow profiles of Figure 8. We find that the flow profile fluctuates quite significantly in unsteady structures: the width of the plate shear layers and the strength vary by factors of 2 or 3; the number of shear bands jumps between 1 and 3; and the mid-gap is sometimes in strong shear and others in nearly plug flow. Evidence of a non-monotone flow profile is evident in one of the snapshots, a phenomenon seen by Sebastian Heidenreich in related studies and in full kinetic flow-nematic simulations of Ruhai Zhou (private communications).

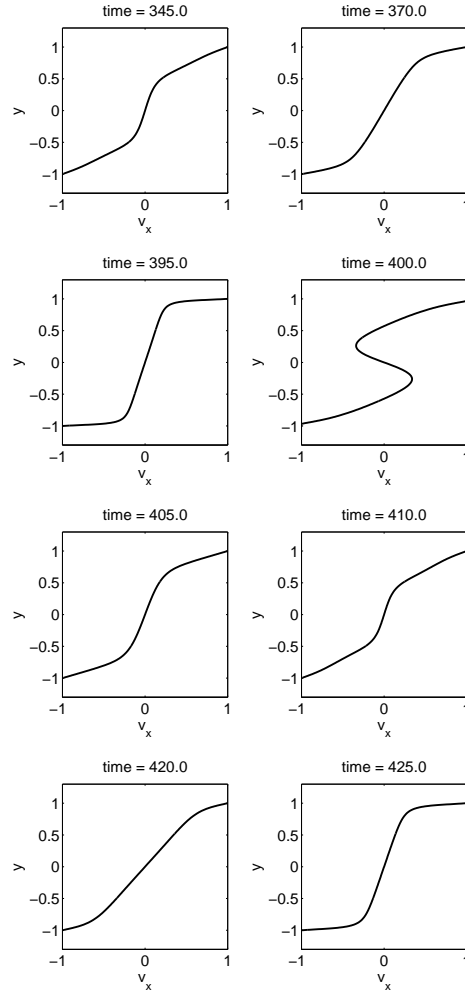


FIGURE 15. Eight more snapshots of flow profiles across the gap corresponding to Fig. 13.

These jet-like layers, which we find in more dramatic fashion below (Figure 15), deserve further study.

5.2. Er cascade for $Pe = 0.5$ and normal anchoring. In **Figure 10**, we compare both in-plane and out-of-plane unsteady solutions for normal anchoring condition with $Er = 100$ and 1000 , respectively. The in-plane (solid red) flow profiles in the top row are analogous to the model 2d liquid results of Kupferman et al. [28]. One observes the generation of shear bands which increase in number as Er increases. To see the evolution of shear band generation, **Figure 11** provides 4 snapshots at each Ericksen number, for both in-plane and out-of-plane attractors. The shear bands again fluctuate in number, strength and location across the gap. The surface plots in Figure 10 indicate a dynamic process of shear band propagation, collisions, reformation, and eventual settling at long times into a time-periodic structure. The vorticity evolution for the out-of-plane simulations, Row 3 of Figure

10, shows fluctuations in vorticity which appear to have lower amplitudes at higher Er .

The detailed snapshots in Figure 11 also reveal that confined in-plane simulations predict an overestimate of shear layer strengths and of the number of shear bands in the long-time behavior. The out-of-plane attractors have softened shear layers, where small scale shear bands are basically smoothed out and replaced by larger scale averaged structures. These simulations further show that the plate plug flow layers associated with normal anchoring are much smaller than in steady structures are lower Er . Thus, once the flow becomes unsteady, the bulk flow profile fluctuates between a nearly linear bulk shear flow ($t = 700$) and a nonlinear shear flow with 4 shear bands across the gap ($t = 300, 500$).

5.3. Steady states and unsteady transitions at $Pe = 1$, $Er = 10$. Short of a full attractor phase diagram versus (Er, Pe) and anchoring angle, we show the analogous steady structures and unsteady transitions for $Pe = 1$ rather than $Pe = 0.5$ of the previous Figures 2-11. In **Figure 12**, with $Pe = 1$, $Er = 10$, we show the in-plane steady states for 4 anchoring conditions. (NOTE: The tangential anchoring solution for $Pe = 1$ is not shown here, since it has already gone unsteady at Er below 10, rather than above $Er = 20$ at $Pe = 0.5$.) Comparison of Figures 3 and Figure 12 shows the effects of doubling Pe on the tilted and normal anchoring steady structures at $Er = 10$. The major director winds more in each half gap; the order parameters are amplified for all anchoring angles, indicating greater focusing and defocusing of the orientational distribution across the gap, and thus small lengthscales of nematic and molecular elasticity; and the shear band profiles are steeper for each tilted anchoring condition, the normal anchoring condition has spawned another shear band, while the tangential anchoring condition has gone through an unsteady transition.

The unsteady Er transition for $Pe = 1$ has therefore shifted below 10, whereas it was above $Er = 20$ for $Pe = 0.5$. Our final figures highlight the unsteady attractor for tangential anchoring at $Er = 10$, $Pe = 1$, **Figure 13** and **Figure 14** show an unsteady in-plane attractor which results from the full out-of-plane unsteady code! Thus, at different Pe , clearly the unsteady attractor transition is not simply from an out-of-plane steady state to an out-of-plane unsteady state. We do not present the steady out-of-plane structures versus Er at $Pe = 1$ for tangential anchoring, but clearly there is evidence of the full tensor system having in-plane steady attractors.

This result is consistent with the monodomain bifurcation diagram in Forest and Wang [12] which shows a critical plate speed (there, a Deborah number) at which the tumbling monodomain limit cycle becomes stable in the full orientation tensor dynamics. Thus, bi-stable in-plane tumbling and out-of-plane kayaking monodomains would suggest the possibility of bi-stable steady state structures. The full steady state structure phase diagram will complete this story, which is beyond the present paper. We remark that the non-dimensionalization in the present paper and [12] is different, so a direct comparison requires some effort.

Some additional features of the unsteady attractor are shown in Figure 14 and **Figure 15**. The first normal stress difference (Figure 14, Row 1) fluctuates about zero across the gap, remaining in the negative range near the plates. This negative first normal stress difference is the classical signature of the unsteady shear regime of nematic polymers, and one of the key successes of the Doi theory applied to monodomains. The shear stress (Figure 14, Row 2) varies in space and time, seemingly tracking the times at which shear layers are the strongest (as expected). The

unsteady flow profile (Figure 14, Row 3) shows an important feature: the near plate flow profile is plug-like as opposed to the steady profiles for tangential anchoring which all exhibit plate shear layers. Finally, the orientation tensor uniquely defines a triaxial ellipsoid, which for in-plane tensors has major axis in the shear plane. Figure 14, Row 4 shows 3 snapshots of the orientation tensor ellipsoid projected on the shear plane. The nematic elasticity is sometimes almost negligible, but then there are collective tumbling events across the gap which generate director distortions. Note the ellipses near the plates have less eccentricity, signaling lower values of the order parameters s , and therefore a defocusing of the orientational distribution. Finally, the 8 snapshots of the flow profile are shown in Figure 15, indicating once again the variability in the bulk flow across the gap. The most dramatic profile occurs at $t = 400$, showing an extreme illustration of non-monotone primary velocity structure, with twin jet-like layers in either half of the shear gap. This corresponds in the flow surface plot Figure 13 to the bulge visible at this time. We strongly suspect that these 1d flow-nematic structures are unstable to 2d spatial perturbations, which is a topic of present study in our group.

6. Concluding remarks. We have employed a mesoscopic Doi-Marrucci-Greco model for the orientation tensor and the unsteady Stokes momentum balance to study 1d heterogeneity of flowing nematic polymers in plane Couette cells. This numerical continuation study has revealed several phenomena relevant to nematic polymers materials: unsteady structure transitions may be activated by device controls, molecular properties, and plate anchoring controls. Furthermore, a remarkable shear band structure is revealed, marked by anchoring-tuned steady flow profiles at low Er and Pe , replaced as either Er or Pe is increased by a transition to unsteady flow-orientation response in steady operating conditions. The dynamic flow profiles are remarkable in that they fluctuate at fixed material and experimental conditions in the strength, number, and location of shear bands through the plate gap. These studies only expose the diversity of phenomena that are possible in flow-nematic interactions. A more detailed phase diagram for these parameter studies, and the extensions to higher space dimensions, are presently under study in our research group.

Acknowledgements. Effort sponsored in part by the Air Force Office of Scientific Research, grants FA9550-06-1-0063, FA9550-05-1-0025, F1ATA06313G003, NSF grants DMS-0626180, DMS-0604891, NASA URETI BMat Award NCC-1-02037, and the Army Research Office, grant W911NF-04-D-004.

REFERENCES

- [1] G. Berry, "Texture Development in the Shear Flow of Nematic Solutions of Rodlike Polymers," Keynote Lecture, Japan Society of Materials Science, Osaka Japan, June, 2001.
- [2] W. R. Burghardt, *Molecular orientation and rheology in sheared lyotropic liquid crystalline polymers*, Macromol. Chem. Phys., **199** (1998), 471–488.
- [3] T. Carlsson, *Theoretical investigation of the shear flow of nematic liquid crystals with the Leslie viscosity $\alpha > 0$: hydrodynamic analogue of first order phase transitions*, Mol. Cryst. Liq. Cryst., **104** (1984), 307–334.
- [4] T. Carlsson, *Unit-sphere description of nematic flows*, Physical Review A, **34** (1986), 3393–3404.
- [5] P.E. Cladis and S. Torza, in "Colloid and Interface Science," **4** (1976), M. Kelker, Editor, Academic Press, NY.
- [6] Z. Cui, M. G. Forest, Q. Wang and H. Zhou, *On weak plane Couette and Poiseuille flows of rigid rod and platelet ensembles*, SIAM J. Appl. Math., **66** (2006), 1227–1260.

- [7] P.G. de Gennes, "The Physics of Liquid Crystals," Clarendon Press, 1974.
- [8] A. M. Donald and A. H. Windle, "Liquid Crystalline Polymers," Cambridge Solid State Science Series, Cambridge University Press, 1992.
- [9] J. L. Ericksen, *Liquid crystals with variable degree of orientation*, Arch. Ration. Mech., **113** (1991), 97–120.
- [10] J. Feng, G. Sgulari and L. G. Leal, *A theory for flowing nematic polymers with orientational distortion*, J. Rheol., **44** (2000), 1085–1101.
- [11] J. Feng, J. Tao and L. G. Leal, *Roll cells and disclinations in sheared polymer nematics*, J. Fluid Mech., **449** (2001), 179–200.
- [12] M. G. Forest and Q. Wang, *Monodomain response of finite-aspect-ratio macromolecules in shear and related linear flows*, Rheol. Acta, **42** (2003), 20–46.
- [13] M. G. Forest, Q. Wang and H. Zhou, *Nonhomogeneous patterns with core defects in elongational flows of liquid crystal polymers*, J. Rheol., **43** (1999), 1573–1582.
- [14] M. G. Forest, Q. Wang and H. Zhou, *Homogeneous biaxial patterns and director instabilities of liquid crystal polymers in axial and planar elongation*, Phys. Fluids, **12** (2000), 490–498.
- [15] M. G. Forest, Q. Wang and H. Zhou, *Exact banded patterns from a Doi-Marrucci-Greco model of nematic liquid crystal polymers*, Physical Review E, **61** (2000), 6655–6662.
- [16] M.G. Forest, Q. Wang and H. Zhou, *Methods for the exact construction of mesoscale spatial structures in liquid crystal polymers*, Physica D, **152–153** (2001), 288–309.
- [17] M. G. Forest, R. Zhou and Q. Wang, *Full-tensor alignment criteria for sheared nematic polymers*, Journal of Rheology, **47** (2003), 105–127.
- [18] M.G. Forest, Wang, Q., H. Zhou and R. Zhou, *Structure scaling properties of confined nematic polymers in plane Couette cells: The weak flow limit*, J. Rheol., **48** (2004), 175–192.
- [19] M.G. Forest, Q. Wang and R. Zhou, *The weak shear kinetic phase diagram for nematic polymers*, Rheol. Acta., **43** (2004), 17–37.
- [20] M.G. Forest, Q. Wang and R. Zhou, *The flow-phase diagram of Doi-Hess theory for sheared nematic polymers II: finite shear rates*, Rheol. Acta., **44** (2004), 80–93.
- [21] M. G. Forest, R. Zhou and Q. Wang, *Kinetic structure simulations of nematic polymers in plane Couette cells, II: In-plane structure transitions*, SIAM Multiscale Modeling and Simulation, **4** (2005), 1280–1304 .
- [22] M. G. Forest, R. Zhou, Q. Wang, X. Zheng and R. Lipton, *Anisotropy and heterogeneity of nematic polymer nano-composite film properties*, IMA, **141** (2005), Modeling of soft matter, 85–98.
- [23] K. Hongladarom, W. R. Burghardt, *Molecular alignment of polymer liquid crystals in shear flows. 2. Transient flow behavior in poly (benzyl glutamate) solutions*, Macromolecules, **26** (1993), 785–794 .
- [24] K. Hongladarom, V. M. Ugaz, D. K. Cinader, W. R. Burghardt, J. P. Quintana, B. S. Hsiao, M. D. Dadmun, W. A. Hamilton and P. D. Butler, *Birefringence, X-Ray scattering and neutron scattering measurements of molecular orientation in sheared liquid crystal polymer solutions*, Macromolecules, **29** (1996), 5346–5355.
- [25] I.G. Kevrekidis, C.W. Gear and C. Theodoropoulos, *Perspective equation-free: The computer-aided analysis of complex multiscale systems*, AIChE Journal, **50** (2004), 1346–1355.
- [26] D.H. Klein, C.J. Garcia-Cervera, H.D. Ceniceros and L.G. Leal, *Computational studies of the shear flow behavior of a model for nematic liquid crystalline polymers*, ANZIAM J., **46** (2005), C210–C244 .
- [27] D.H. Klein, C.J. Garcia-Cervera, H.D. Ceniceros and L.G. Leal, *Ericksen number and Deborah number cascade predictions of a model for liquid crystalline polymers for simple shear flow*, Physics of Fluids, **19** (2007), 023101.
- [28] R. Kupferman, M. Kawaguchi and M. M. Denn, *Emergence of structure in a model of liquid crystalline polymers with elastic coupling*, J. Non-Newt. Fluid Mech., **91** (2000), 255–271.
- [29] R. G. Larson, "The Structure and Rheology of Complex Fluids," Oxford University Press, 1999.
- [30] R. G. Larson and D. W. Mead, *Development of orientation and texture during shearing of liquid crystalline polymers*, Liq. Cryst., **12** (1993), 751–768.
- [31] R. G. Larson and D. W. Mead, *The Ericksen number and Deborah number cascade in sheared polymeric nematics*, Liq. Cryst., **15** (1993), 151–169.
- [32] R. G. Larson and H. Ottinger, *The effect of molecular elasticity on out-of-plane orientations in shearing flows of liquid crystalline polymers*, Macromolecules, **24** (1991), 6270–6282 .

- [33] F. M. Leslie, *Theory of Flow Phenomena in Liquid Crystals*, Advances in Liquid Crystals, **4** (1979), 1–81.
- [34] P. L. Maffettone and S. Crescitelli, *Bifurcation analysis of a molecular model for nematic polymers in shear flows*, J. Non-Newtonian Fluid Mech., **59** (1995), 73–91.
- [35] P. Manneville, *The transition to turbulence in nematic liquid crystals: Part 1, general review. Part 2, on the transition via tumbling*, Mol. Cryst. Liq. Cryst., **70** (1981), 223–250.
- [36] G. Marrucci, *Tumbling regime of liquid-crystalline polymers*, Macromolecules, **24** (1991), 4176–4182.
- [37] G. Marrucci and F. Greco, *The elastic constants of Maier-Saupe rodlike molecular nematics*, Mol. Cryst. Liq. Cryst., **206** (1991), 17–30.
- [38] G. Marrucci and F. Greco, *Flow behavior of liquid crystalline polymers*, Adv. Chem. Phys. (edited by I. Prigogine and S. Rice.), **86** (1993), 331–404.
- [39] P. T. Mather, D. Pearson and R. G. Larson, *Flow patterns and disclination-density measurements in sheared nematic liquid crystals*, Liq. Cryst., **20** (1996), 527–538.
- [40] P.T. Mather, A. Romo-Uribe, C. D. Han and S. S. Kim, *Rheo-optical evidence of a flow-induced isotropic-nematic transition in a thermotropic liquid-crystalline polymer*, Macromolecules, **30**, (1997), 7977–7989.
- [41] A.D. Rey and M.M. Denn, *Dynamical phenomena in liquid-crystalline materials*, Annual Rev. Fluid Mech., **34** (2002), 233–266.
- [42] G. Sgalari, G. L. Leal and J. Feng, *The shear flow behavior of LCPs based on a generalized Doi model with distortional elasticity*, J. Non-Newtonian Fluid Mechanics, **102** (2002), 361–382.
- [43] A. P. Singh and A. D. Rey, *Microstructure constitutive equation for discotic nematic liquid crystalline materials*, Rheol. Acta, **37** (1998), 30–45.
- [44] M. Srinivasarao and G. C. Berry, *Rheo-optical studies on aligned nematic solutions of a rodlike polymer*, J. Rheol., **35** (1991), 379–397.
- [45] Z. Tan and G. C. Berry, *Studies on the texture of nematic solutions of rodlike polymers, 3. Rheo-optical and rheological behavior in shear*, J. Rheol., **47** (2003), 73–104.
- [46] T. Tsuji and A. D. Rey, *Effect of long range order on sheared liquid crystalline polymers, Part 1: compatibility between tumbling behavior and fixed anchoring*, J. Non-Newt. Fluid Mech., **73** (1997), 127–152.
- [47] T. Tsuji and A. D. Rey, *Orientation mode selection mechanisms for sheared nematic liquid crystalline materials*, Phys. Rev. E, **57** (1998), 5609–5625.
- [48] Q. Wang, *Biaxial steady states and their stability in shear flows of liquid crystal polymers*, J. Rheol., **41** (1997), 943–970.
- [49] Q. Wang, *A hydrodynamic theory for solutions of nonhomogeneous nematic liquid crystalline polymers of different configuration*, J. Chem Phys., **116** (2002), 9120–9136.
- [50] X. Zheng, M. G. Forest, R. Lipton, R. Zhou and Q. Wang, *Exact scaling laws for electrical conductivity properties of nematic polymer nano-composite monodomains*, Adv. Func. Mat., **15** (2005), 627–638.
- [51] X. Zheng, M. G. Forest, R. Lipton and R. Zhou, *Nematic polymer mechanics: flow-induced anisotropy*, *Continuum Mechanics and Thermodynamics*, to appear.
- [52] X. Zheng, M. G. Forest, R. Vaia, M. Arlen and R. Zhou, *Shear-guided anisotropic geometrical percolation in nano-rod ensembles*, X. J. Applied Physics, submitted November, 2006.
- [53] H. Zhou and M.G. Forest, *Anchoring distortions coupled with plane Couette & Poiseuille flows of nematic polymers in viscous solvents: morphology in molecular orientation, stress & flow*, Discrete and Continuous Dynamical Systems, **6** (2006), 407–425.
- [54] H. Zhou and M.G. Forest, *Nematic liquids in weak capillary Poiseuille flow: structure scaling laws and effective conductivity implications*, International Journal of Numerical Analysis and Modeling, **4** (2007), 460–477.
- [55] R. Zhou, M. G. Forest and Q. Wang, *Kinetic structure simulations of nematic polymers in plane Couette cells, I: The algorithm and benchmarks*, SIAM Multiscale Modeling and Simulation, **3** (2005), 853–870.

Received October 2006; revised May 2007.

E-mail address: hzhou@nps.edu

E-mail address: forest@email.unc.edu

E-mail address: wang@math.fsu.edu